Testing Symmergent gravity through the shadow image and weak field photon deflection by a rotating black hole using the M87* and Sgr. A* results

Reggie C. Pantig,^{1,*} Ali Övgün,^{2,†} and Durmuş Demir^{3,‡}

¹Physics Department, De La Salle University, 2401 Taft Avenue, Manila, 1004 Philippines

²Physics Department, Eastern Mediterranean University,
Famagusta, 99628 North Cyprus via Mersin 10, Turkey

³Faculty of Engineering and Natural Sciences, Sabancı University, 34956 İstanbul, Turkey

(Dated: October 18, 2022)

Motivated by recent work on the symmergent black hole [Phys. Dark Univ. 10.1016/j.dark.2021.100900, 2021], here we study spinning black holes in symmergent gravity, with spin parameter a. The goal is to uncover the deviations caused by the symmergent gravity parameters relative to the known Kerr solution. To this aim, we first investigate the deviations in the photon sphere and shadow size. The EHT data is used to determine constraints on $c_{\rm O}$ that fit well in M87* within $\pm 1\sigma$ than in Sgr. A*. In view of the quadratic curvature coefficient co, the symmergent gravity mimics dS and AdS spacetimes in regard to the conditions $\hat{\alpha} > 1$, and $\hat{\alpha} < 1$, which is an integration constant. Depending on these conditions, we observe deviations in the photonsphere radius and the shadow radius. Also, we find that the geodesics of time-like particles are more sensitive to symmergent gravity effects than the null geodesics. Finally, we also analyze the weak field limit of the deflection angles, where we use the Gauss-Bonnet theorem by taking into account the finite distance of the source and the receiver to the lensing object. Remarkably, the distance of the receiver (or source) from the lensing object greatly influences the deflection angle. The quadratic curvature coefficient c_0 , which is proportional to the number difference between fermions and bosons, needs to be negative for a consistent solution. To complete the picture, we analyze also symmergent gravity effects when the rotating black hole acts as a particle accelerator. Overall, our multi-faceted analysis shows that symmergent gravity can be probed via different black hole observables.

PACS numbers: 95.30.Sf, 04.70.-s, 97.60.Lf, 04.50.Kd

Keywords: Black hole; Modified gravity; Geodesics; Weak gravitational lensing; Shadow; Deflection angle.

I. INTRODUCTION

In this work, we test a recent emergent gravity model with the shadow and deflection angle of rotating black holes using the observational data on the M87* and SgrA* black holes. The emergent gravity model we study exhibits distinctive signatures, as we have revealed in recent work on static black hole spacetimes [1]. It is expected that the rotating black hole spacetimes can act as a richer laboratory to test or explore the emergent gravity model we consider.

Fundamentally, quantum field theory (QFT), with mass and spin of each field being Casimir invariants, is intrinsic to flat spacetime simply because it rests on a Poincaré-invariant (translation-invariant) vacuum state [2, 3]. Flat spacetime means the total absence of gravity. Incorporation of gravity necessitates the QFT to be transferred to curved spacetime, but this is hampered by Poincaré breaking in curved spacetime [3, 4]. This obstacle plus absence of a quantum theory of gravity [5] leads one to emergent gravity scheme [6–8] as a viable framework.

In general, loss of Poincaré invariance could be interpreted as the emergence of gravity into the QFT [9]. In a QFT, the curvature can emerge through Poincaré breaking sources, for which one obvious candidate is the hard momentum cutoff. Indeed, an ultraviolet (UV) cutoff Λ [10] limits momenta p_{μ} within $-\Lambda^2 \leq \eta^{\mu\nu}p_{\mu}p_{\nu} \leq \Lambda^2$ interval as the intrinsic validity edge of the QFT [10]. It gives cause to scalar masses $(c_S\Lambda^2)$ and vacuum energy $(c_mm^2\Lambda^2+c_O\Lambda^4)$ at the loop level. It also gives cause to gauge boson masses $(c_V\Lambda^2)$ [11, 12], which break gauge symmetries explicitly since Λ is not a particle mass, that is, Λ is not a Casimir invariant of the Poincaré group. In Sakharov's induced gravity, Λ^2 is associated with the Planck scale, albeit with explicitly-broken gauge symmetries and Planckian-size cosmological constant and scalar masses.

In recent years, the induced gravity setup of Sakharov has been approached from a new perspective in which priority is given to the resolution of the explicit gauge symmetry breaking [13]. In parallel with the introduction of Higgs field to restore gauge symmetry for a massive vector boson (with Casimir invariant mass) [14–16], spacetime affine curvature is introduced to restore gauge symmetries for gauge bosons with loop-induced (Casimir non-invariant) masses proportional to Λ [13, 17, 18]. This way, general relativity emerges holographically via the affine dynamics such that loop-induced gauge boson

^{*} reggie.pantig@dlsu.edu.ph

[†] ali.ovgun@emu.edu.tr; https://www.aovgun.com

[‡] durmus.demir@sabanciuniv.edu

masses get erased, and scalar masses get stabilized by the curvature terms. This mechanism renders effective field theories natural regarding their destabilizing UV sensitivities [13, 17]. It gives rise to a new framework in which (i) its gravity sector is composed of the Einstein-Hilbert term plus a curvature-squared term, and (ii) its matter sector is an \overline{MS} -renormalized QFT [13]. This framework possesses distinctive signatures that can be searched via astrophysical, cosmological, and collider experiments. Its gravity sector, a symmetry-restoring emergent gravity theory briefly termed as "symmergent gravity" [17, 18], is composed entirely of loop-induced couplings, including the Newton's constant G.

It is worth noting that symmergent gravity is not a loop-induced curvature sector in curved spacetime [7, 19]. In contrast, the flat spacetime effective field theory is taken to curved spacetime [13, 17] in a way reviving the gauge symmetries broken explicitly by the UV cutoff. All of its couplings are loop-induced parameters deriving from the particle spectrum of the QFT (numbers and masses of particles). With respect to the standard model of known particles (leptons, quarks, gauge bosons, and the Higgs boson), correct induction of the Newton's constant bring about a plethora of new particles which, unlike supersymmetry or other well-known models, do not have to couple to the known particles. Using Occam's razor and stability of the Higgs boson mass, this freedom means that new particles do not couple to the known particles unless they are required to couple observationally or experimentally [13, 20]. To exemplify this, one expects neutrinos to be Dirac since only such neutrinos keep the Higgs boson mass stable. The symmergent gravity has already been studied in certain aspects. Its quadratic-curvature sector, different than that in Sakharov's induced gravity [7, 19], has already been shown to give rise to the Starobinsky inflation [21]. The same quadratic curvature sector has recently been shown to possess distinctive signatures for the black hole shadow [1]. In more recent work, the symmergent gravity has been studied in detail in the quasi-periodic oscillations, weak field lensing, and shadow cast around static black hole spacetimes [22]. We shall study symmergent gravity in spinning black hole spacetimes in the present work. Our study (like the earlier ones [1, 21, 22]) can be viewed as "doing particle physics via black holes" as it will reveal salient properties of the QFT sector through various black hole features.

In 1919 Arthur Eddington led an expedition to prove Einstein's theory of relativity using gravitational lensing and since then lensing has become an important tool in astrophysics [23–32]. In astrophysics, distances are very important when determining the properties of astrophysical objects. But Virbhadra showed that just the observation of relativistic images without any information about the masses and distances can also accurately give value of the upper bound on the compactness of massive dark objects [33]. Furthermore, Virbhadra proved that there exists a distortion parameter such that the signed sum of all images of singular gravitational lensing of a source identically vanishes (tested with Schwarzschild lensing in weak and strong gravitational fields [34]).

In 2008, Gibbons and Werner used the Gauss-Bonnet theorem (GBT) on the optical geometries in asymptotically flat spacetimes, and calculated weak deflection angle for first time in literature [35]. Afterwards, this method has been applied to various phenomena [36–49]. One of the aims of the present paper is to probe symmergent gravity through the black hole's weak deflection angle using the GBT and also the shadow silhouette as perceived by a static remote observer. In essence, by the very nature of the symmergent gravity, we will be studying the numbers of fermions and bosons and related effects in the vicinity of a spinning black hole, which has the potential to affect the motions of null and time-like geodesics as well as their spin parameter a. (By definition, $a = cJ/GM^2$ where J and M are the angular momentum and mass of the rotation black hole.) Recently, shadow coming from different black hole models has been analyzed extensively in the literature as a probe of the imprints of the astrophysical environment affecting it [50–97] Calculation of the shadow cast of a non-rotating black hole was pioneered by [98] and [99], and later on extended by [100] [101] to an axisymmetric spacetime. Recently, after the detection of gravitational waves in 2015 [102], the first image of the black hole in M87* was formed by the Event Horizon Telescope (EHT) using its electromagnetic spectrum [103]. At the time of writing of this paper, new milestone has been achieved since the EHT revealed the shadow image of the black hole in our galaxy, Sgr. A* [104]. This new result indicates that black hole theory and phenomenology is a hot research topic in vivew of the rapidly developing observational techniques.

The paper is organized as follows. In Sec. II, we briefly discuss the symmergent gravity. We give in Sec. III the rotating metric, indicating dependence on the symmergent parameters. In Sec. IV, we study the effects of symmergent gravity on null geodesics, which in turn influence the shadow radius and observables associated with it. We also examine the said effect on time-like orbits in the same section. We devote Sec. V to investigation of the weak deflection angle at finite-distance, and in Sec. VI we calculate the center-of-mass energy (CM) of two particles and study particle acceleration near rotating symmergent black hole background. In Sec. VII, we conclude and give future prospects. Throughout the paper we use natural units by setting G = c = 1, and the metric signature (-, +, +, +).

II. SYMMERGENT GRAVITY

Symmergent gravity is essentially an $R+R^2$ gravity theory with cosmological constant. It can be regarded as a special form of general f(R) gravity theories. It has been constructed in complete detail in [13] (see also [17, 18] for earlier discussions). It has recently been summarized in [1, 22] in regard to its implications for black features like quasi-periodic

oscillations, shadow radius, and weak lensing. These studies on symmergent black holes already give the relevant details about the curvature sector of symmergent gravity. Below, we briefly discuss its relevant features.

The action functional of the symmergent gravity is given by

$$S[g] = \int d^4x \sqrt{-g} \left\{ \frac{R(g)}{16\pi G} - \frac{c_{\rm O}}{16} R(g)^2 - V_{\rm O} + \mathcal{L}_{matter} \right\}$$
 (1)

in which \mathcal{L}_{matter} is that part which involves the known matter fields (quarks, leptons, gauge bosons and the Higgs) in the standard model plus the new fields needed to induce Newton's constant in the form

$$\frac{1}{G} = \frac{\text{str}\left[\mathcal{M}^2\right]}{8\pi} \tag{2}$$

where $\mathrm{str}[\dots]$ stands for the graded trace $\mathrm{str}[\mathcal{M}^2] = \sum_s (-1)^s \, \mathrm{tr}[\mathcal{M}^2]_s$, with s being the particle spin and \mathcal{M}^2 the mass-squared matrix of all the matter fields. Not only the Newton's constant G_N but also the quadratic curvature coefficient c_{O} and the vacuum energy density V_{O}

$$c_{\rm O} = \frac{n_{\rm B} - n_{\rm F}}{128\pi^2} \,, \ V_{\rm O} = \frac{\text{str}\left[\mathcal{M}^4\right]}{64\pi^2}$$
 (3)

are loop-induced parameters such that $n_{\rm B}$ ($n_{\rm F}$) stands for the total number of bosons (fermions) in the underlying QFT. Both the $n_{\rm B}$ bosons and $n_{\rm F}$ fermions contain not only the known standard model particles but also the completely new particles (massive as well as massless) that do not have to couple to the known particles non-gravitationally.

Before indulging into the analysis of the quadratic-curvature action (1) one notes that if nature contains equal numbers of the bosonic and fermionic degrees of freedom (namely, $n_{\rm B}=n_{\rm F}$) then $c_{\rm O}\equiv 0$. Then symmetric gravity reduces to general relativity (with non-minimal couplings to scalars S in the theory). This bose-fermi symmetric structure is a property of the supersymmetric theories. Interestingly, symmetric predicts pure Einstein gravity when $n_{\rm B}=n_{\rm F}$ in nature, with the further property that extra particles do not have to interact with the known particles. In this case, one obtains the usual asymptotically-flat Schwarzschild or Kerr black holes.

The symmergent gravity action (1) can be put into the form

$$S = \frac{1}{16\pi G} \int d^4x \sqrt{-g} \left(R(g) + f(R(g)) + 16\pi G \mathcal{L}_{matter} \right) \tag{4}$$

in which

$$f(R) = -\pi G c_{\rm O} R(g)^2 - 16\pi G V_{\rm O}$$
(5)

stands for the terms beyond the linear Einstein-Hilbert term. Then, from (4) follows the equation of motion

$$R_{\mu\nu}(1+f'(R)) - \frac{1}{2}g_{\mu\nu}(R+f(R)) + (\nabla_{\mu}\nabla_{\nu} - \Box g_{\mu\nu})f'(R) + 8\pi G T_{\mu\nu} = 0$$
 (6)

in which $T_{\mu\nu}$ is the energy-momentum tensor of matter fields contained in \mathcal{L}_{matter} . We look for a constant-curvature solution, $R=R_0$. To this end, in the absence of matter, we find the relation [105, 106]

$$R_0 = \frac{2f(R_0)}{f'(R_0) - 1} \tag{7}$$

with the solution

$$R_0 = 32\pi G V_{\rm O} \tag{8}$$

which would vanish if the vacuum energy were not nonzero. As follows from its definition in equation (3), the vacuum energy can be analyzed as follows

$$V_{\rm O} = \frac{\text{str}\left[\mathcal{M}^{4}\right]}{64\pi^{2}} = \frac{1}{64\pi^{2}} \left(\sum_{\rm B} m_{\rm B}^{4} - \sum_{\rm F} m_{\rm F}^{4}\right)$$

$$\leq \frac{1}{64\pi^{2}} \left(\left(\sum_{\rm B} m_{\rm B}^{2}\right)^{2} - \left(\sum_{\rm F} m_{\rm F}^{2}\right)^{2}\right)$$

$$= \frac{1}{64\pi^{2}} \left(\sum_{\rm B} m_{\rm B}^{2} - \sum_{\rm F} m_{\rm F}^{2}\right) \left(\sum_{\rm B} m_{\rm B}^{2} + \sum_{\rm F} m_{\rm F}^{2}\right)$$
(9)

$$= \frac{1}{8\pi G} \left(\sum_{\mathbf{B}} m_{\mathbf{B}}^2 + \sum_{\mathbf{F}} m_{\mathbf{F}}^2 \right)$$

where in the last line we used the formula for Newton's constant (2). In fact, the formula for Newton's constant suggests that $(n_{\rm B}-n_F)\left(\sum_{\rm B}m_{\rm B}^2+\sum_{\rm F}m_{\rm F}^2\right)\sim 1/8\pi G$, as can be seen by going to the complete mass degeneracy limit. This rough relationship can be utilized to put the vacuum energy in the form

$$V_{\rm O} = \frac{1 - \hat{\alpha}}{(8\pi G_N)^2 c_{\rm O}} \tag{10}$$

by setting $(n_{\rm B}-n_{\rm F})\left(\sum_{\rm B}m_{\rm B}^2+\sum_{\rm F}m_{\rm F}^2\right)=(1-\hat{\alpha})16\pi G^{-1}$ such that $\hat{\alpha}\neq 1$ is a constant parametrizing how close $(n_{\rm B}-n_{\rm F})\left(\sum_{\rm B}m_{\rm B}^2+\sum_{\rm F}m_{\rm F}^2\right)$ is to Newton's constant.

Under the vacuum energy formula in (10), the curvature scalar in (8) takes the form

$$R_0 = \frac{1 - \hat{\alpha}}{2\pi G c_{\Omega}} \tag{11}$$

and it leads to the static metric [105, 106]

$$ds^{2} = -h(r)dt^{2} + \frac{dr^{2}}{h(r)} + r^{2}(d\theta^{2} + \sin^{2}\theta d\phi^{2})$$
(12)

with a lapse function

$$h(r) = 1 - \frac{2GM}{r} - \frac{1 - \hat{\alpha}}{24\pi Gc_0} r^2 \tag{13}$$

involving the symmergent gravity parameters $c_{\rm O}$ and $\hat{\alpha}$. To summarize, the symmergent gravity gives the vacuum energy in (3), and simple algebraic manipulations in (9) and (10) lead to the constant scalar curvature in (11) and the metric function in (13).

III. ROTATING BLACK HOLES IN SYMMERGENT GRAVITY

Appropriate for a rotating black hole geometry, we use Boyer-Lindquist coordinates with a metric free of the coordinate singularities in the spacetime both exterior to the black hole and interior to the cosmological horizon. The metric is given by [105, 107–111]

$$ds^{2} = \frac{\rho^{2}}{\Delta_{r}} dr^{2} + \frac{\rho^{2}}{\Delta_{\theta}} d\theta^{2} + \frac{\Delta_{\theta} \sin^{2} \theta}{\rho^{2}} \left[a dt - \left(r^{2} + a^{2} \right) \frac{d\phi}{\Xi} \right]^{2} - \frac{\Delta_{r}}{\rho^{2}} \left(dt - a \sin^{2} \theta \frac{d\phi}{\Xi} \right)^{2}$$

$$(14)$$

with the various quantities

$$\Delta_r = (r^2 + a^2) \left(1 - \frac{r^2}{3} \frac{(1 - \hat{\alpha})}{8\pi c_{\rm O}} \right) - 2Mr,$$
(15)

$$\rho^2 = r^2 + a^2 \cos^2 \theta \,, \tag{16}$$

$$\Delta_{\theta} = 1 + \frac{r^2}{3} \frac{(1 - \hat{\alpha})}{8\pi c_{\rm O}} a^2 \cos^2 \theta \,, \tag{17}$$

$$\Xi = 1 + \frac{r^2}{3} \frac{(1 - \hat{\alpha})}{8\pi c_{\rm O}} a^2 \,. \tag{18}$$

Here, a is the black hole spin parameter, and $\hat{\alpha}$ and $c_{\rm O}$ are the parameters of the symmergent gravity. The physical energy E and angular momentum J of the black hole are related to the parameters m and a via the relations [112, 113]

$$E = \frac{m}{\Xi^2}, \quad J = \frac{am}{\Xi^2} \tag{19}$$

in which m is determined by solving the equation $\Delta_r(r_+)=0$, with r_+ standing for the radius of the event horizon. In this way, one can express energy and angular momentum in terms of the parameters r_+ , a, and G. (One here notes that

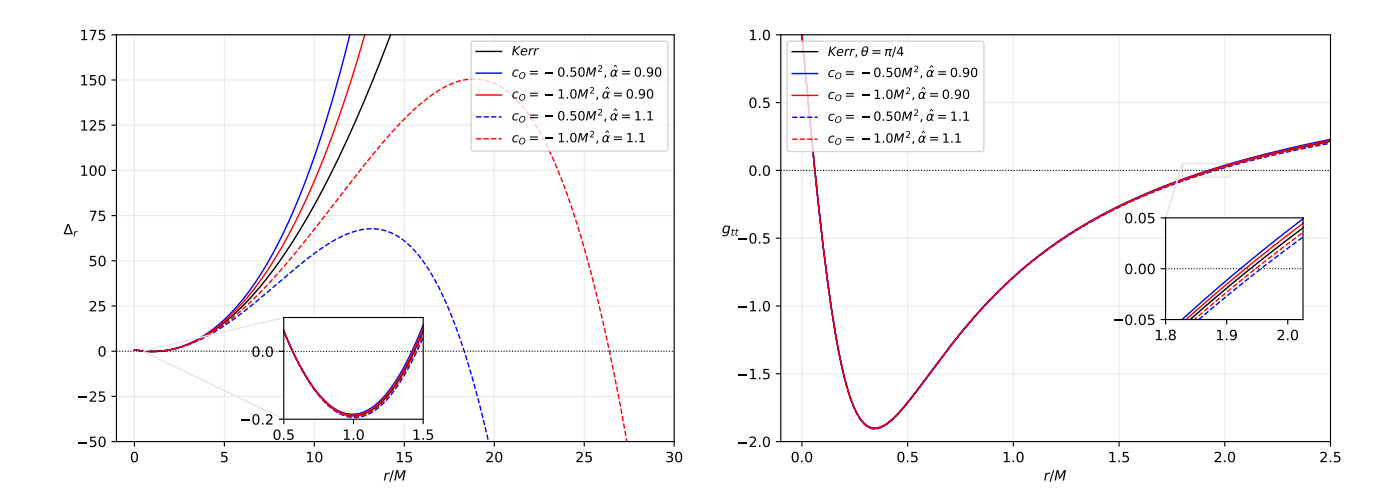


FIG. 1. Variations of the functions Δ_r (left panel) and g_{tt} (right panel) with the radial coordinate r for the black hole spin parameter $a=0.9\,M$. The plots show the null boundaries, with solid (dashed) lines mimicking the behavior of AdS (dS) black holes. We consider only negative values of $c_{\rm O}$ in agreement with [114].

 $\frac{1}{l^2} = \frac{(\hat{a}-1)}{24\pi G_N \, c_{\rm O}}$, where the curvature radius l is related to the negative cosmological constant as $\Lambda = -3l^{-2}$). As a result, one finds

$$E = \frac{1}{2\Xi^2 r_+} \left(r_+^2 + a^2 + \frac{r_+^4}{l^2} + \frac{a^2 r_+^2}{l^2} \right), \quad J = \frac{a}{2\Xi^2 r_+} \left(r_+^2 + a^2 + \frac{r_+^4}{l^2} + \frac{a^2 r_+^2}{l^2} \right) \tag{20}$$

as the explicit expressions for the definitions in (19).

Numerically, horizons can be determined by analyzing the lapse function, that is, by solving $\Delta_r=0$ using its definition in (15). Besides, the location of the ergoregions can be determined numerically by plotting the metric component g_{tt} and looking for points satisfying $g_{tt}=0$. In fact, plotted in Fig. 1 are Δ_r and g_{tt} as functions of r for the integration constant $\hat{\alpha}$ of 0.90 and 1.10, black hole spin parameter $a=0.9\,M$, and the various values of $c_{\rm O}$. In general, symmergent black hole can mimic the dS ($\hat{\alpha}>1$) or AdS-Kerr ($\hat{\alpha}<1$) black holes depending on the sign of $\hat{\alpha}$. But, as already shown by Pogosian and Silvestri [114], consistent f(R) gravity theories require $\frac{dF(R)}{dR}>0$ in order to remain stable the (non-tachyonic scalaron). This constraint imposes the condition $c_{\rm O}<0$ on the loop-induced quadratic curvature coefficient, and restricts viable solutions to the AdS-Kerr type. In view of the underlying QFT, $c_{\rm O}<0$ implies that $n_{\rm F}>n_{\rm B}$ – a mostly fermionic QFT [13, 17, 18]. In the extreme case of no new bosons (in agreement with $n_{\rm F}>n_{\rm B}$), one finds out that the new particle sector remains inherently stable thanks to the fact that fermion masses do not have any power-law sensitivity to the UV cutoff.

Usually, value of the cosmological constant is scaled to a higher value to see its overall effect. In this sense, assumed values of $\hat{\alpha}$ and $c_{\rm O}$ are also rescaled similarly. As is seen from Fig. 1, null boundaries are greatly affected by the values of the symmergent parameters $\hat{\alpha}$ and $c_{\rm O}$. Indeed, $\hat{\alpha}>1$ leads to three horizons where, in the context of the dS geometry, the third horizon corresponds to the cosmic outer boundary. It shifts farther as $c_{\rm O}$ gets more negative. The two remaining null boundaries are the Cauchy and event horizons. In constrast to the dS solution, the symmergent AdS solution gives only two horizons such that symmergent effects are nearly vanishingly small on the inner horizon compared to the outer horizon. As for the ergoregions, $\hat{\alpha}>1$ leads to three ergoregions, and it can be seen that the farthest one turns out to be even beyond the cosmic horizon.

The Hawking temperature is given by

$$T = \frac{\kappa}{2\pi} \tag{21}$$

such that the surface gravity

$$\kappa^2 = -\frac{1}{2} \nabla^\mu \chi^\nu \nabla_\mu \chi_\nu \tag{22}$$

involves the null Killing vectors χ^{ν} . The two Killing vectors $\xi^{\nu} = \partial_t$ and $\zeta^{\nu} = \partial_{\varphi}$ in the metric are associated with the time translation and rotational invariance, respectively. Consequently, we take

$$\chi^{\nu} = \xi^{\nu} + \Omega \zeta^{\nu} \tag{23}$$

and determine Ω under the condition that $\chi^{
u}$ is a null vector. This leads to the constraint

$$\chi^{\nu}\chi_{\nu} = g_{tt} + 2\Omega g_{t\varphi} + \Omega^2 g_{\varphi\varphi} = 0, \tag{24}$$

from which one gets

$$\Omega = -\frac{g_{t\varphi}}{g_{\varphi\varphi}} \pm \sqrt{\left(\frac{g_{t\varphi}}{g_{\varphi\varphi}}\right)^2 - \frac{g_{tt}}{g_{\varphi\varphi}}} \tag{25}$$

which reduces to

$$\Omega_{+} = \frac{a\Xi}{r_{\perp}^2 + a^2} \tag{26}$$

at the event horizon $\Delta\left(r_{+}\right)=0$. For this Ω value one then gets

$$\kappa = \frac{1}{2\left(r_{+}^{2} + a^{2}\right)} \left. \frac{d\Delta_{r}}{dr} \right|_{r=r_{\perp}},\tag{27}$$

for the surface gravity,

$$T = \frac{r_{+}}{4\pi \left(r_{+}^{2} + a^{2}\right)} \left(1 + \frac{a^{2}}{l^{2}} + \frac{3r_{+}^{2}}{l^{2}} - \frac{a^{2}}{r_{+}^{2}}\right) = \frac{3r_{+}^{4} + \left(a^{2} + l^{2}\right)r_{+}^{2} - l^{2}a^{2}}{4\pi l^{2}r_{+}\left(r_{+}^{2} + a^{2}\right)}$$
(28)

for the Hawking temperature, and

$$S = \frac{A}{4} = \frac{\pi \left(r_+^2 + a^2\right)}{\Xi} \tag{29}$$

for the Bekenstein-Hawking entropy. Needless to say, all thermodynamic quantities are necessarily non-negative. The rotating symmergent black hole satisfies therefore the first law of thermodynamics

$$dE = TdS + \Omega dJ \tag{30}$$

with

$$\Omega = \frac{a\left(1 + r_{+}^{2}l^{-2}\right)}{r_{+}^{2} + a^{2}} \,. \tag{31}$$

IV. GEODESICS AROUND ROTATING SYMMERGENT BLACK HOLES

In this section we give a detailed analysis of the geodesics and orbits around the symmergent black holes.

A. Null geodesic and shadow cast

We start the analysis with null geodesics. The Hamilton-Jacobi equation gives

$$\frac{\partial S}{\partial \lambda} = -H,\tag{32}$$

where S is the Jacobi action in terms of the affine parameter λ (proper time) and coordinates x^{μ} . The Hamiltonian is given by

$$H = \frac{1}{2}g^{\mu\nu}\frac{\partial S}{\partial x^{\mu}}\frac{\partial S}{\partial x^{\nu}},\tag{33}$$

in the GR so that

$$\frac{\partial S}{\partial \lambda} = -\frac{1}{2} g^{\mu\nu} \frac{\partial S}{\partial x^{\mu}} \frac{\partial S}{\partial x^{\nu}} \tag{34}$$

as follows from (32) above. Using the separability ansatz for the Jacobi function

$$S = \frac{1}{2}\mu^2\lambda - Et + L\phi + S_r(r) + S_\theta(\theta), \tag{35}$$

with the particle mass μ , one is led to the following first-order motion equations [115]

$$\Sigma \frac{dt}{d\lambda} = \frac{\Xi(r^2 + a^2)P(r)}{\Delta_r} - \frac{\Xi aP(\theta)}{\Delta_{\theta}},$$

$$\Sigma \frac{dr}{d\lambda} = \sqrt{R(r)},$$

$$\Sigma \frac{d\theta}{d\lambda} = \sqrt{\Theta(\theta)},$$

$$\Sigma \frac{d\phi}{d\lambda} = \frac{\Xi aP(r)}{\Delta_r} - \frac{\Xi P(\theta)}{\Delta_{\theta} \sin^2 \theta}$$
(36)

after introducing the functions

$$R(r) = P(r)^{2} - \Delta_{r}(\mu^{2}r^{2} + K),$$

$$P(r) = \Xi E(r^{2} + a^{2}) - \Xi aL,$$

$$\Theta(\theta) = \Delta_{\theta}(K - \mu^{2}a^{2}\cos^{2}\theta) - \frac{P(\theta)^{2}}{\sin^{2}\theta},$$

$$P(\theta) = \Xi(aE\sin^{2}\theta - L).$$
(37)

From the third equation in (36) above, constants of motion can be correlated via the relation $K = \Xi^2 (aE - L)^2$, which is a consequence of a hidden symmetry in the θ -coordinate [115, 116].

First, we study null geodesic and shadow cast for massless particles ($\mu = 0$). Photon circular orbits, which are always unstable, must then satisfy the following condition

$$R(r) = \frac{dR(r)}{dr} \mid_{r=r_0} = 0.$$
 (38)

The null geodesic is important is an important quantity for symmergent black holes. We need, in particular, the photon region in constant r_0 , the so-called photonsphere, which is an unstable orbit. The shadow cast ultimately depends on the photon region. With $\mu=0$, it proves convenient to define these two impact parameters

$$\xi = \frac{L}{E} \quad \text{and} \quad \eta = \frac{K}{E^2}. \tag{39}$$

These parameters are found to possess the following explicit expressions

$$\xi = \frac{\Delta_r'(r^2 + a^2) - 4\Delta_r r}{a\Delta_r'},\tag{40}$$

$$\eta = \frac{-r^4 \Delta_r'^2 + 8r^3 \Delta_r \Delta_r' + 16r^2 \Delta_r (a^2 - \Delta_r)}{a^2 \Delta_r'^2} \tag{41}$$

after a lengthy algebra. The photonsphere radius $r_{\rm ph}$ can then be determined by solving $\eta(r)=0$ for r. The analytical solutions are well-known for both Schwarzschild and Kerr black holes. In our case, we plot (41) in Fig. 2 to get the qualitative impression about the location of $r_{\rm ph}$. The left panel of Fig. 2 concerns location of the photonsphere along the equatorial plane. As we would expect, the Schwarzschild case gives $r_{\rm ph}=3M$. The extreme Kerr case gives two possible locations, that is, the prograde orbit at $r_{\rm ph}=M$ and the retrograde orbit at $r_{\rm ph}=4M$. The plot shows the locations for a=0.90M, which fall near the said extreme values. For the symmergent effect, the dS type (dashed lines) gives slightly lower values in the retrograde case while the AdS type gives a larger one. It is clear that the more negative the $c_{\rm O}$ the closer the photon ring to the Kerr case. The symmergent effect is also present in the prograde case though the deviation is smaller than in the retrograde case. In the right panel of Fig. 2, we consider photons with zero angular momentum, that is, those that traverse the equatorial plane in a perpendicular manner (the so-called nodes). The retrograde case gives higher values for such an orbit than the prograde case. The deviation caused is barely evident, especially in the prograde case (the inset highlights the deviation). As a final remark, we note that the symmergent effect mimics dS or AdS cases, where such a behavior does not occur in the Schwarzschild case. The coupling between the spin and symmergent parameters made it possible to affecy the behavior of the photonsphere.

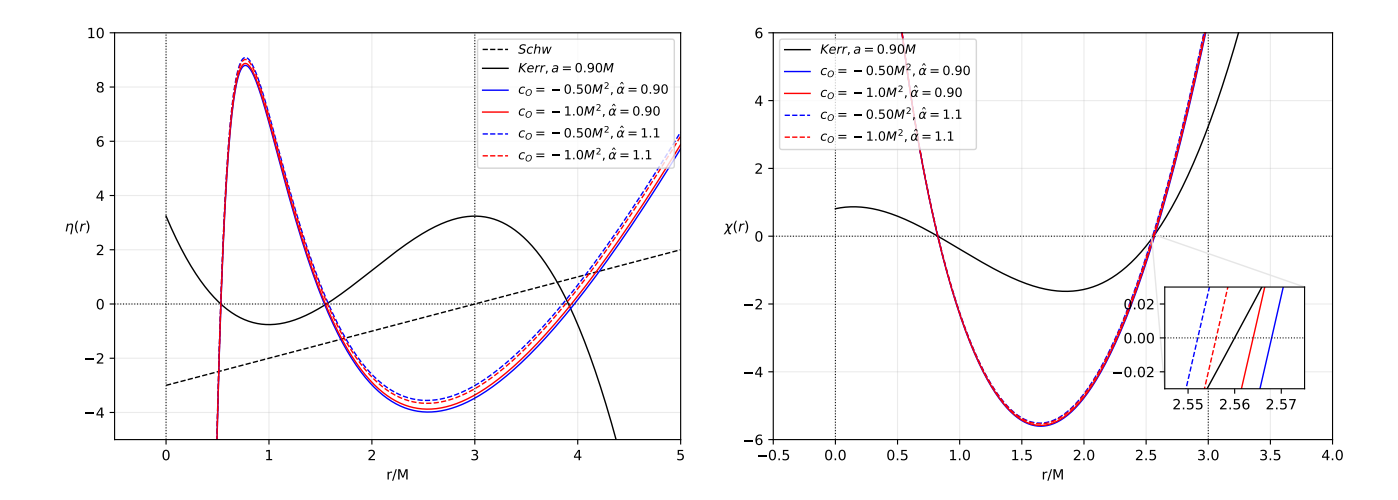


FIG. 2. Location of the photonsphere (left panel), and location of the photonsphere crossing at $\phi = 0$ or along the equatorial plane (right panel). We take a = 0.90M in both plots (a is the black hole spin parameter).

Escaping photons in the unstable orbit gives the possibility for remote observers to backward-trace and obtain a shadow cast by using the celestial coordinates $(r_{\text{obs}}, \theta_{\text{obs}})$. Such an observer is also known as the Zero Angular Momentum Observer (ZAMO). Also, in this type of co-moving frame, without loss of generality, one makes the approximation $r_{\text{obs}} \to \infty$ and takes $\theta_{\text{obs}} = \pi/2$. The celestial coordinates are defined as [117]

$$\alpha = -r_{\text{obs}} \frac{\xi}{\zeta \sqrt{g_{\phi\phi}} \left(1 + \frac{g_{t\phi}}{g_{\phi\phi}} \xi \right)},$$

$$\beta = r_{\text{obs}} \frac{\pm \sqrt{\Theta(i)}}{\zeta \sqrt{g_{\theta\theta}} \left(1 + \frac{g_{t\phi}}{g_{\phi\phi}} \xi \right)},$$
(42)

and the condition $r_{\sf obs} o \infty$ leads to the simplified relations

$$\alpha = -\xi \csc \theta_{\text{obs}},$$

$$\beta = \pm \sqrt{\eta + a^2 \cos^2 \theta_{\text{obs}} - \xi^2 \cot^2 \theta_{\text{obs}}}.$$
(43)

These expressions further simplify to $\alpha=0$ and $\beta=\pm\sqrt{\eta}$ when $\theta_{\rm obs}=\pi/2$. If, furthermore, a=0 then shadow cast of a Schwarzschild black hole (a circle) is obtained. The plot of β vs. α is shown in Fig. 3 for the black hole spin parameter value of a=0.90M. Overall, we observe the D-shaped nature of the shadow cast due to the spin parameter. Considering first the effect of the inclination angle, we see that as we decrease the value of θ (going up from the equatorial plane), we see that the shape changes. Remarkably, in the upper right figure, the shape becomes more compressed in the α axis, and as one continues to go up (lower left figure), it goes back to an almost spherical shape. Finally, near the pole, a drastic change in the shadow shape occurs due to stretching of the α -axis. For the symmergent effects, we note that the dS type tends to decrease the photonsphere radius. Nevertheless, as photons travel in the intervening space under the effect of the symmergent parameter the shadow size is seen to increase. We can see the contrast in the AdS type symmergent effect in that while the photonsphere increases the shadow size tends to decrease.

In the azimuthal plane, we see how the shadow becomes "D-shaped" when the balck hole spin parameter a is near extremal. The numerical value of the shadow radius associated with this shape [52, 73] can be calculated [53] by using

$$R_{\mathsf{s}} = \frac{\beta_{\mathsf{t}}^2 + (\alpha_{\mathsf{t}} - \alpha_{\mathsf{r}})^2}{2|\alpha_{\mathsf{t}} - \alpha_{\mathsf{r}}|} \tag{44}$$

which we plot in Fig. 4 (upper left), along with the shadow's angular radius θ_{sh} (upper right), where the latter is defined by

$$\theta_{\rm sh} = 9.87098 \times 10^{-3} \frac{R_{\rm s}M}{D} \tag{45}$$

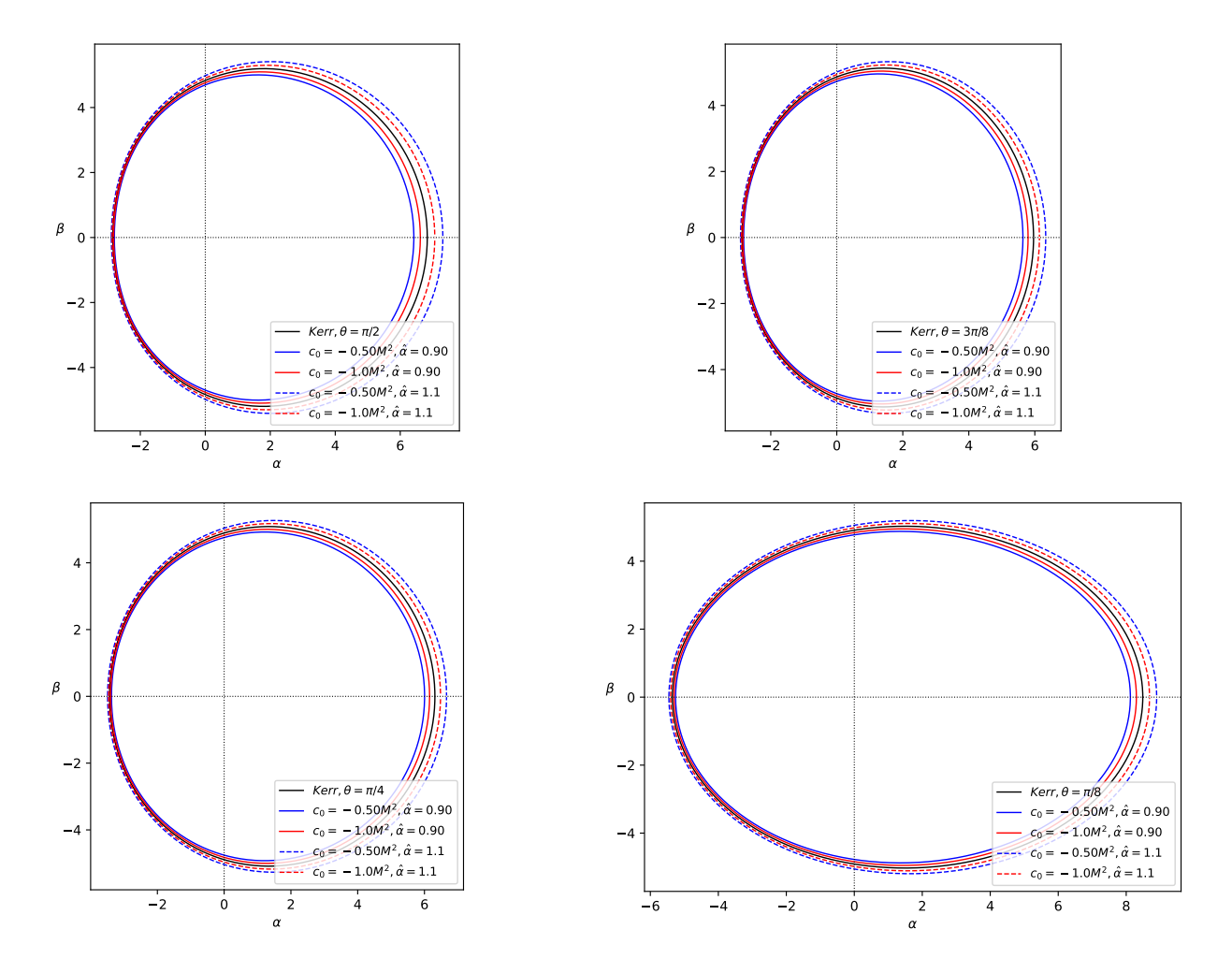


FIG. 3. Shadow plot for different inclination angles for the black hole spin parameter a=0.90M (aspect ratios of figures are set to obtain the actual view).

after taking the black hole mass M in units of M_{\odot} and D in parsecs. We emphasize that these behaviors are consistent with Fig. 3. Other observables that can be derived from the shadow are the distortion parameter $\delta_{\rm s}$ and the energy emission rate $\frac{d^2E}{d\omega dt}$, which are defined as

$$\delta_{\mathsf{s}} = \frac{d_{\mathsf{s}}}{R_{\mathsf{s}}} = \frac{\tilde{\alpha}_{\mathsf{l}} - \alpha_{\mathsf{l}}}{R_{\mathsf{s}}},\tag{46}$$

$$\frac{d^2E}{d\omega dt} = 2\pi^2 \frac{\Pi_{ilm}}{e^{\omega/T} - 1} \omega^3 \tag{47}$$

such that the energy absorption cross-section can be approximated as $\Pi_{ilm} \sim \pi R_{\rm s}^2$ for an observer at $r_{\rm obs} \to \infty$. These observables are plotted in Fig. 4 in the lower two panels. From these panels we are able to see how the spin parameter increases the distortion of the shadow. We can also see that even if the dS symmergent effect tends to increase the shadow, the distortion it gives is smaller than the AdS symmergent effect. In the lower right panel of Fig. 4, we comparatively show a=0.25M and a=0.90M for the Kerr, dS and AdS symmergent black holes. For the Kerr case, we see that low values of a leads to higher values for energy emission rate and peak frequency. Adding the symmergent effect at low values of a and a=0.90, we see that a less negative a=0.90 provides the highest peak frequency and energy emission rate. For a=0.90 in the inset plot that the roles are reversed near the peak of the curve. We see that there is a point in the plot where the behavior flips as the frequency a=0.90 increases whilst the emission rate decreases.

We now investigate observational constraints on the symmetre $c_{\rm O}$ using the black hole shadow data collected from M87* [118] and Sgr. A* [104]. The data is tabulated in Table I. With these data, one can determine diameter of the

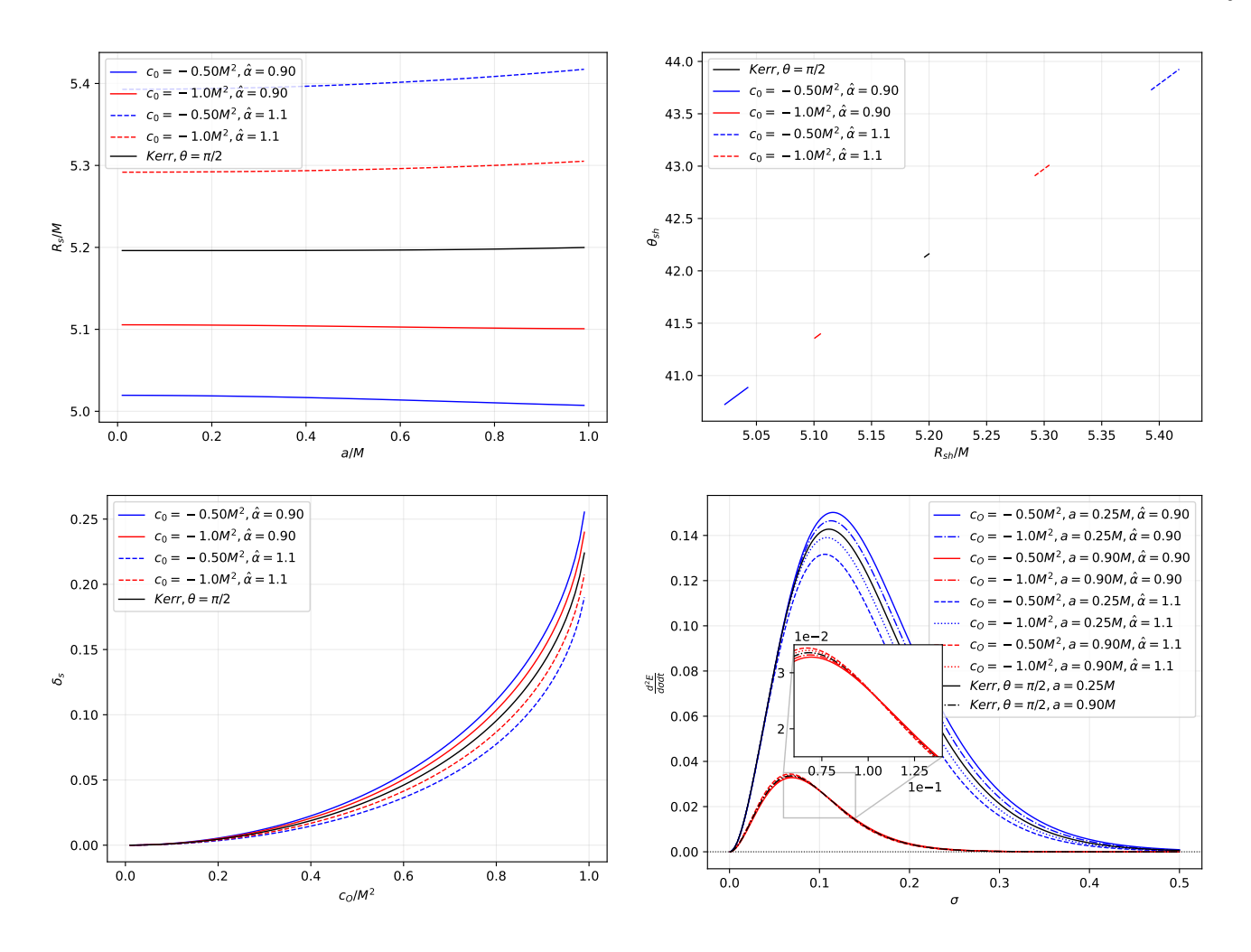


FIG. 4. Shadow observables associated with the upper left panel of Fig. 3. Shown here are shadow radius (upper-left panel), angular diameter in μ as for M87* (upper-right panel), distortion parameter (lower-left panel), and energy emission rate (lower-right panel).

Black hole	Mass (M_{\odot})	Angular diameter: $2\theta_{\sf sh}$ (μ as)	Distance (kpc)
Sgr. A*	4.3 ± 0.013 x 10^{6} (VLTI)	48.7 ± 7 (EHT)	8.277 ± 0.033
M87*	$6.5 \pm 0.90 \times 10^9$	42 ± 3	16800

TABLE I. Black hole observational constraints.

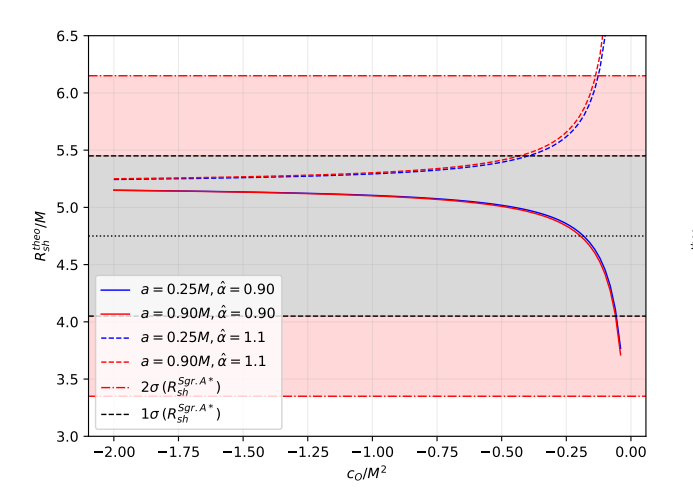
shadow size in units of the black hole mass with

$$d_{\mathsf{sh}} = \frac{D\theta}{M}.\tag{48}$$

In this sense, the diameter of the shadow image of M87* and Sgr. A* are $d_{\rm sh}^{\rm M87*}=(11\pm1.5)m$ and $d_{\rm sh}^{\rm Sgr. A*}=(9.5\pm1.4)m$, respectively. Meanwhile, the theoretical shadow diameter can be obtained via $d_{\rm sh}^{\rm theo}=2R_{\rm sh}$ with the use of equation (44). Based on Fig. 5, we can conclude that the parameters we used in describing the shadow cast fall within the upper and lower bounds at the 1σ level. Where this happens, the range in $c_{\rm O}$ is more extensive in M87* than in Sgr. A*. We also observe that less negative $c_{\rm O}$ introduces more sensitivity to deviation than more negative $c_{\rm O}$.

B. Symmergent gravity effects on time-like orbits: Effective potential and ISCO radii

We now turn our attention to time-like orbits. Here, we will still use the equations of motion from the Hamilton-Jacobi approach but this time set $\mu = 1$. We are interested in determining the radius of the innermost stable circular orbit (ISCO),



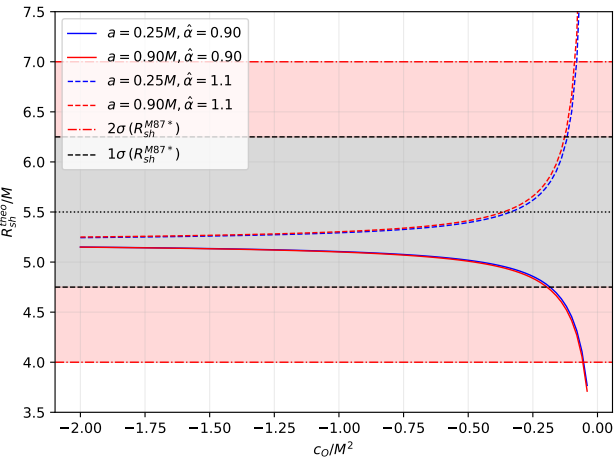


FIG. 5. Constraint on the symmergent gravity parameter $c_{\rm O}$ by the Sgr. A* data (left-panel) and M87* data (right-panel).

Sgr. A*	2σ		1σ		observed $R_{\sf sh}$
$spin \ a \ (\hat{\alpha} = 0.90)$	upper	lower	upper	lower	mean
0.25M	-	-	-	-0.057	-0.184
0.90M	-	-	-	-0.060	-0.196
$spin \ a \ (\hat{\alpha} = 1.10)$	upper	lower	upper	lower	mean
0.25M	-0.127	-	-0.397	-	-
0.90M	-0.137	-	-0.431	-	-

M87*	2σ		1σ		observed $R_{\sf sh}$
$\frac{1}{\text{spin } a \ (\hat{\alpha} = 0.90)}$	upper	lower	upper	lower	mean
0.25M	-	-0.054	-	-0.196	-
0.90M	-	-0.057	-	-0.185	-
spin a ($\hat{\alpha} = 1.10$)	upper	lower	upper	lower	mean
0.25M	-0.081	-	-0.117	-	-0.336
0.90M	-0.089	-	-0.128	-	-0.364

TABLE II. Bounds on c_0 as read off from the curves in Fig. 5.

which is very important in the study of matter accretion disks and in the study also of the effective potential for getting a qualitative description of bound and unbound orbits under the symmergent effects.

To determine the qualitative behavior of massive particle's motion around the symmergent black hole (i.e. bound, stable and unstable circular orbits), we use the effective potential formula [119]

$$V_{\pm} = \frac{g^{t\phi}}{g^{tt}} L \pm \left\{ \left[\left(\frac{g^{t\phi}}{g^{tt}} \right)^2 - \frac{g^{\phi\phi}}{g^{tt}} \right] L^2 - \frac{1}{g^{tt}} \right\}^{1/2}. \tag{49}$$

written in terms of the inverse metric $g^{\mu\nu}$ and angular momentum L. Shown in Fig. 6 is the effective potential for $L=\pm 3.50M$. In this figure, maxima and minima correspond to the unstable and stable circular orbits, respectively. One notes that for a=0 (Schwarzschild) case, the maxima of the effective potential curve are way lower compared to when a=0.90M (Kerr case). We can see that the energy for an unstable circular orbit is higher in the AdS symmergent effect, where less negative c_0 giving the highest energy. Its minima, which represents the stable circular orbit, has a greater radius for more negative c_0 . Peculiar as it may seem, particles with energies higher that than the peak energy tend to get deflected back when it reaches at some radial point near the cosmic horizon (one recalls that we scaled the Symmergent dS and AdS parameters). As for the dS symmergent effect, we can see that the least negative c_0 gives the lowest peak energy in the unstable circular orbit. Particles with low energy are deflected back to $r\to\infty$ when they reach low values of r. While the AdS type can have elliptical bound orbits the same way as in the Kerr case, we see that dS type does not admit such orbit as far as the value of the angular momentum used herein is concerned. In Fig. 6 (right-panel), we plotted also the effective potential in which the particle attains a negative angular momentum. It is known that it does not happen in the Schwarzschild case. As we can see in the right-panel, particles with negative energies can be created near the rotating black hole's event horizon. Clearly, symmergent gravity affects the particle's energy, which in turn contributes to the Penrose process and black hole evaporation.

The ISCO radius occurs when the maximum and minimum of the effective potential curve merge in an inflection point for a given value of L. It is clear that we have two separate cases for ISCO determination since we need to consider both the prograde and retrograde motion of the time-like particles. Besides, such a circular orbit is only marginally stable, which means that any inward perturbation will lead the particle to spiral toward the event horizon. In locating the ISCO radius, we

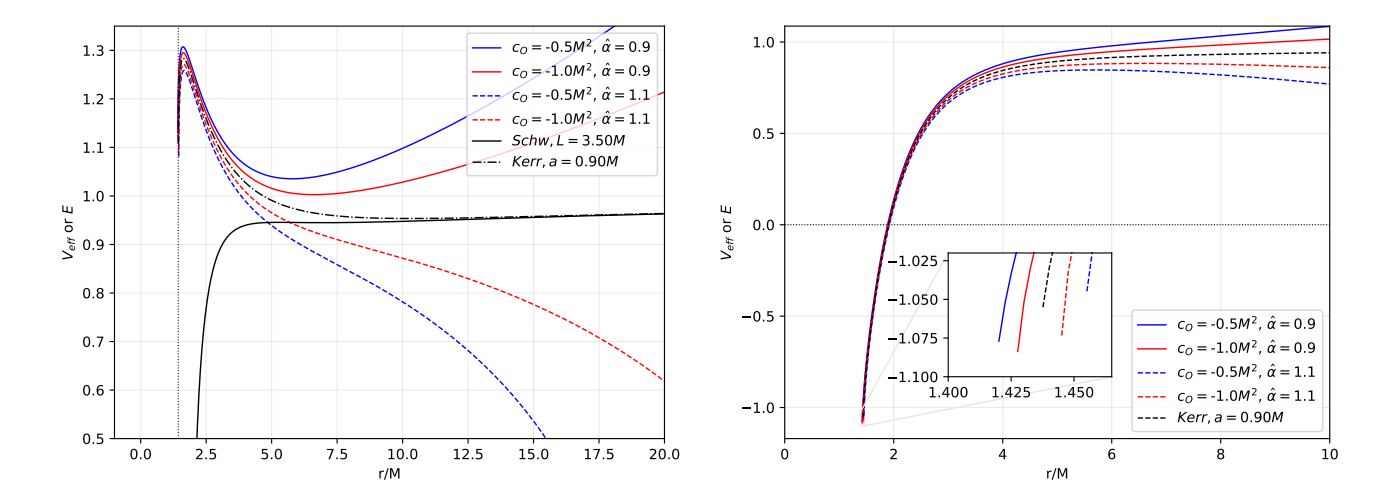


FIG. 6. The effective potential as a function of r/M for L>0 (left-panel) and L<0 (right-panel). In both plots, the black hole spin parameter is set to a=0.90M.

use equation (38) and solve for the energy E_{cir} . One starts with [115, 120]

$$X^{2} = L - aE = \frac{r^{3} \left(\Delta_{r}^{\prime} - 2E_{\text{cir}}^{2} r\right)}{-2a^{2} - r\Delta_{r}^{\prime} + 2\Delta_{r}}.$$
(50)

Differentiating equation (50) with respect to r and after some algebra we get ($E_{cir} = E_{isco}$)

$$E_{\rm isco}^2 = \frac{1}{Br} \left\{ a^2 \left[-\left(r\Delta_r'' + 3\Delta_r'\right) \right] + r\Delta_r \Delta_r'' - 2r\Delta_r'^2 + 3\Delta_r \Delta_r' \right\},\tag{51}$$

where $B=-8a^2+r\left(r\Delta_r''-5\Delta_r'\right)+8\Delta_r$. The ISCO radius can then be found by solving the equation [52]

$$\eta(r)_{\text{isco}} = \pm 2\Delta_r \left(a^2 - \Delta_r\right)^2 \pm \frac{9}{4} r \Delta_r \left(a^2 - \Delta_r\right) \Delta_r' \pm \frac{1}{16} r^3 \Delta_r' \left(\Delta_r \Delta_r'' - 2\Delta_r'^2\right)
\pm \frac{1}{16} r^2 \left[4\Delta_r \left(a^2 - \Delta_r\right) \Delta_r'' + \left(15\Delta_r - 4a^2\right) \Delta_r'^2\right]
+ a\Delta_r \sqrt{4a^2 + 2r\Delta_r' - 4\Delta_r} \left[-a^2 + \frac{1}{8} r \left(r\Delta_r'' - 5\Delta_r'\right) + \Delta_r\right] = 0$$
(52)

which redues to the Kerr case

$$3a^2 \mp 8a\sqrt{m}\sqrt{r} + r(6m - r) = 0 \tag{53}$$

when $\Delta(r)=r^2-2mr+a^2$. The upper and lower signs in equation (52) correspond to the prograde and retrograde orbit of the massive particle at the ISCO radius, respectively. We determine ISCO radius numerically by plotting equation (52) in Fig. 7. First, we note that in the Schwarzschild case, the ISCO radius is located at r=6M. For the extreme Kerr case, on the other hand, the prograde ISCO is at r=M (which coincides with the prograde photonsphere) and retrograde ISCO is at r=9M. Thus, in Fig. 7, the left-panel represents the retrograde ISCO where we can see clearly how the symmergent parameters affect the radius. The innermost radius, which determines the accretion disk's innermost region, is smaller in the AdS type whilst the dS type is slightly larger in the Kerr case. We note that the first root of $\eta_{\rm isco}$ is unphysical since those radii are smaller than the photonsphere in the retrograde case. Finally, we see the same symmergent effects in the prograde ISCO (right-panel of Fig. 7). Before we close this section, we remark that we used lower values of c_0 in time-like geodesics than when analyzing the null boundaries and geodesics. Thus, there must be some different constraints to be considered in studying time-like geodesics. If we used the same parameters for the null case, the results would be unphysical. Nonetheless, even if c_0 are more negative, we see that time-like particles are more sensitive to symmergent effects.

V. WEAK DEFLECTION ANGLE FROM ROTATING SYMMERGENT BLACK HOLES USING GAUSS-BONNET THEOREM

In this section, we investigate the deflection angle of light rays from the rotating symmergent black hole in the weak field limit using the methodology given in [41, 43]. Below, we briefly discuss the finite distance method. First of all, the

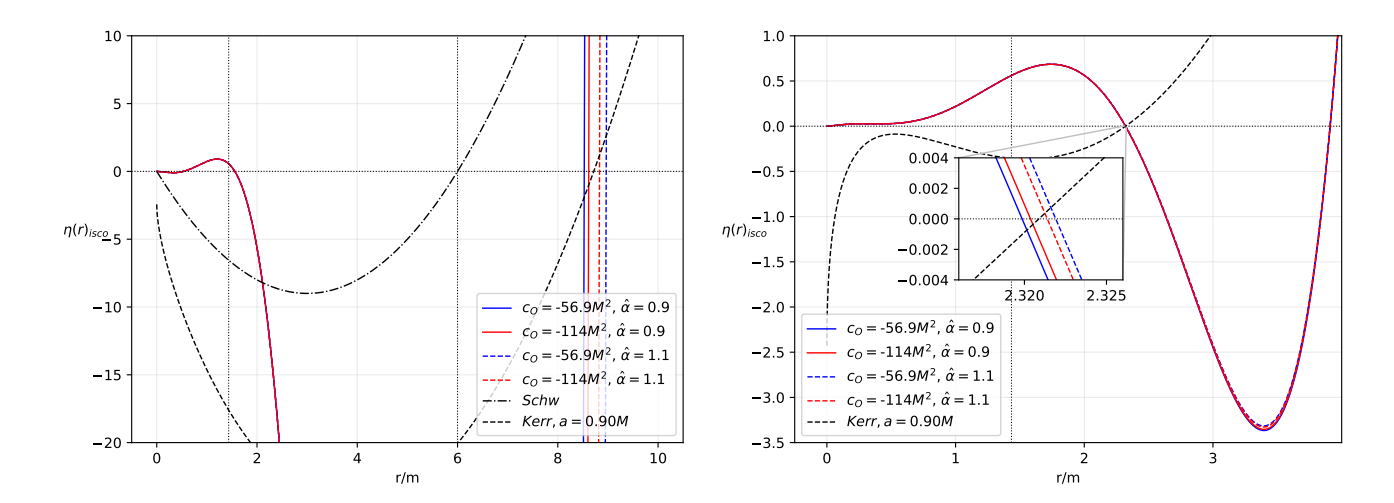


FIG. 7. Location of ISCO radius for counter-rotation of a massive particle (left-panel) and co-rotation of a massive particle (right-panel). We set a=0.90M in both panels.

deflection angle is defined as

$$\Theta = \Psi_{\mathsf{R}} - \Psi_{\mathsf{S}} + \phi_{SR} \tag{54}$$

in which ϕ_{SR} is the longitude separation angle, Ψ_{R} is the angle between light rays and radial direction, and Ψ_{S} is the angle between the observer and the source. Unit tangential vector e^{i} is used to write the above angle as follows

$$(e^r, e^\theta, e^\phi) = \epsilon \left(\frac{dr}{d\phi}, 0, 1\right) \tag{55}$$

where ϵ is a radial quantity. For a stationary spacetime described by the metric

$$ds^{2} = -A(r,\theta)dt^{2} + B(r,\theta)dr^{2} + C(r,\theta)d\theta^{2} + D(r,\theta)d\phi^{2} - 2H(r,\theta)dtd\phi,$$
(56)

one straightforwardly finds

$$\epsilon = \frac{A(r)D(r) + H^{2}(r)}{A(r)(H(r) + A(r)b)},\tag{57}$$

where b is the impact parameter. We can write conserved quantities energy and the angular momentum per unit mass in the form

$$E = A(r)\dot{t} + H(r)\dot{\phi} \qquad L = D(r)\dot{\phi} - H(r)\dot{t},\tag{58}$$

where the overdot denotes the derivative of the coordinates t and ϕ with respect to the affine parameter λ (proper time). In the equatorial plane $(\theta = \frac{\pi}{2})$, the line element reduces to

$$dl^2 \equiv \gamma_{ij} dx^i dx^j \tag{59}$$

with the spatial metric γ_{ij} . It is then possible to define

$$\cos \Psi \equiv \gamma_{ij} e^i R^j. \tag{60}$$

as the angle between the direction e^i and the radial vector $R^j = (\frac{1}{\sqrt{\gamma_{rr}}}, 0, 0)$. Having $\cos \Psi$ at hand, we use equations (55) and (60) to get

$$\sin \Psi = \frac{H(r) + A(r)b}{\sqrt{A(r)D(r) + H^2(r)}}.$$
(61)

Now, using this methodology we can calculate the deflection angle of the symmergent black hole in the weak field limit. Indeed, with the impact parameter $b=\frac{L}{E}$ and radial coordinate 1/u in place of r we get

$$\left(\frac{du}{d\phi}\right)^2 = \frac{1}{b^2} - \frac{4aMu}{b^3} - u^2 + 2Mu^3 + \frac{1-\hat{\alpha}}{24\pi c_0} - \frac{2a}{3b^3u^2} \frac{(1-\hat{\alpha})}{8\pi c_0} - \frac{8aM}{3b^3u} \frac{(1-\hat{\alpha})}{8\pi c_0} + \mathcal{O}\left[M^2, \left(\frac{1-\hat{\alpha}}{8\pi c_0}\right)^2, a^2\right]$$
(62)

where we considered only the retrograde solution. For the prograde solution, we just flip the sign of the spin parameter a. It is convenient to start by computing the separation angle integral. This can be done by writing $\left(\frac{du}{d\phi}\right)^2=F(u)$ and extracting the angle

$$\phi_{RS} = \int_{S}^{R} d\phi = \int_{u_{S}}^{u_{0}} \frac{1}{\sqrt{F(u)}} du + \int_{u_{R}}^{u_{0}} \frac{1}{\sqrt{F(u)}} du, \tag{63}$$

where $u_{\rm S}$ ($u_{\rm R}$) is inverse distance to the source (observer), and u_0 is the inverse of the closest approach r_0 . Considering the weak field and slow rotation approximations, the impact parameter can be related to u_0 as

$$b = \frac{1}{u_0} + M - 2aMu_0 + \mathcal{O}\left[M^2, \left(\frac{1-\hat{\alpha}}{8\pi c_0}\right)^2, a^2\right].$$
 (64)

Then, performing the necessary calculations we find

$$\begin{split} \phi_{\text{RS}} &= \phi_{\text{RS}}^{\text{Kerr}} + \left(\frac{u_{\text{R}}}{\sqrt{1 - b^2 u_{\text{R}}^2}} + \frac{u_{\text{S}}}{\sqrt{1 - b^2 u_{\text{S}}^2}}\right) \frac{b^3}{6} \frac{(1 - \hat{\alpha})}{8\pi c_0} + \left(\frac{b\left(2 - 3b^2 u_{\text{R}}^2\right)}{2\left(1 - b^2 u_{\text{R}}^2\right)^{3/2}} + \frac{b\left(2 - 3b^2 u_{\text{S}}^2\right)}{2\left(1 - b^2 u_{\text{S}}^2\right)^{3/2}}\right) \frac{M}{3} \frac{(1 - \hat{\alpha})}{8\pi c_0} \\ &+ \left(\frac{1 - 2b^2 u_{\text{R}}^2}{u_{\text{R}}\sqrt{1 - b^2 u_{\text{R}}^2}} + \frac{1 - 2b^2 u_{\text{S}}^2}{u_{\text{S}}\sqrt{1 - b^2 u_{\text{S}}^2}}\right) \frac{a}{3} \frac{(1 - \hat{\alpha})}{8\pi c_0} + \mathcal{O}\left[M^2, \left(\frac{1 - \hat{\alpha}}{8\pi c_0}\right)^2, a^2\right], \end{split} \tag{65}$$

where the Kerr term is given by

$$\phi_{\text{RS}}^{\text{Kerr}} = \phi_{\text{RS}}^{\text{SW}} - \left(\frac{1}{\sqrt{1 - b^2 u_{\text{R}}^2}} + \frac{1}{\sqrt{1 - b^2 u_{\text{S}}^2}}\right) \frac{2aM}{b^2}.$$
 (66)

In this equation, the Schwarzschild term is

$$\phi_{\text{RS}}^{\text{Schw}} = \pi - \arcsin(bu_{\text{R}}) - \arcsin(bu_{\text{S}}) + \left(\frac{2 - b^2 u_{\text{R}}^2}{\sqrt{1 - b^2 u_{\text{R}}^2}} + \frac{2 - b^2 u_{\text{S}}^2}{\sqrt{1 - b^2 u_{\text{S}}^2}}\right) \frac{M}{b}.$$
 (67)

To get the remaining terms appearing in the light deflection angle expression, one should identify the Ψ terms. We find

$$\sin \Psi = bu - bMu^2 + 2aMu^2 - \left(\frac{bM}{6} - \frac{a}{3u} + \frac{b}{6u}\right) \frac{(1-\hat{\alpha})}{8\pi c_0} + \mathcal{O}\left[M^2, \left(\frac{1-\hat{\alpha}}{8\pi c_0}\right)^2, a^2\right].$$
 (68)

This relation produces

$$\begin{split} \Psi_{\mathsf{R}} - \Psi_{\mathsf{S}} &= \Psi_{\mathsf{R}}^{\mathsf{Kerr}} - \left(\frac{1}{u_{\mathsf{R}}\sqrt{1 - b^2 u_{\mathsf{R}}^2}} + \frac{1}{u_{\mathsf{S}}\sqrt{1 - b^2 u_{\mathsf{S}}^2}}\right) \frac{b}{6} \frac{(1 - \hat{\alpha})}{8\pi c_0} - \left(\frac{2b^2 u_{\mathsf{R}}^2 - 1}{(1 - b^2 u_{\mathsf{R}}^2)^{3/2}} + \frac{2b^2 u_{\mathsf{S}}^2 - 1}{(1 - b^2 u_{\mathsf{S}}^2)^{3/2}}\right) \frac{bM}{6} \frac{(1 - \hat{\alpha})}{8\pi c_0} \\ &+ \left(\frac{1}{u_{\mathsf{R}}\sqrt{1 - b^2 u_{\mathsf{R}}^2}} + \frac{1}{u_{\mathsf{S}}\sqrt{1 - b^2 u_{\mathsf{S}}^2}}\right) \frac{a}{3} \frac{(1 - \hat{\alpha})}{8\pi c_0} + \mathcal{O}\left[M^2, \left(\frac{1 - \hat{\alpha}}{8\pi c_0}\right)^2, a^2\right], \end{split} \tag{69}$$

where one has

$$\Psi_{\mathsf{R}}^{\mathsf{Kerr}} - \Psi_{\mathsf{S}}^{\mathsf{Kerr}} = \Psi_{\mathsf{R}}^{\mathsf{Schw}} - \Psi_{\mathsf{R}}^{\mathsf{Schw}} + \left(\frac{u_{\mathsf{R}}^2}{\sqrt{1 - b^2 u_{\mathsf{R}}^2}} + \frac{u_{\mathsf{S}}^2}{\sqrt{1 - b^2 u_{\mathsf{S}}^2}}\right) 2aM,\tag{70}$$

and where one has found

$$\Psi_{\mathsf{R}}^{\mathsf{Schw}} - \Psi_{\mathsf{R}}^{\mathsf{Schw}} = \left(\arcsin(bu_{\mathsf{R}}) + \arcsin(bu_{\mathsf{S}}) - \pi\right) - \left(\frac{u_{\mathsf{R}}^2}{\sqrt{1 - b^2 u_{\mathsf{R}}^2}} + \frac{u_{\mathsf{S}}^2}{\sqrt{1 - b^2 u_{\mathsf{S}}^2}}\right) Mb. \tag{71}$$

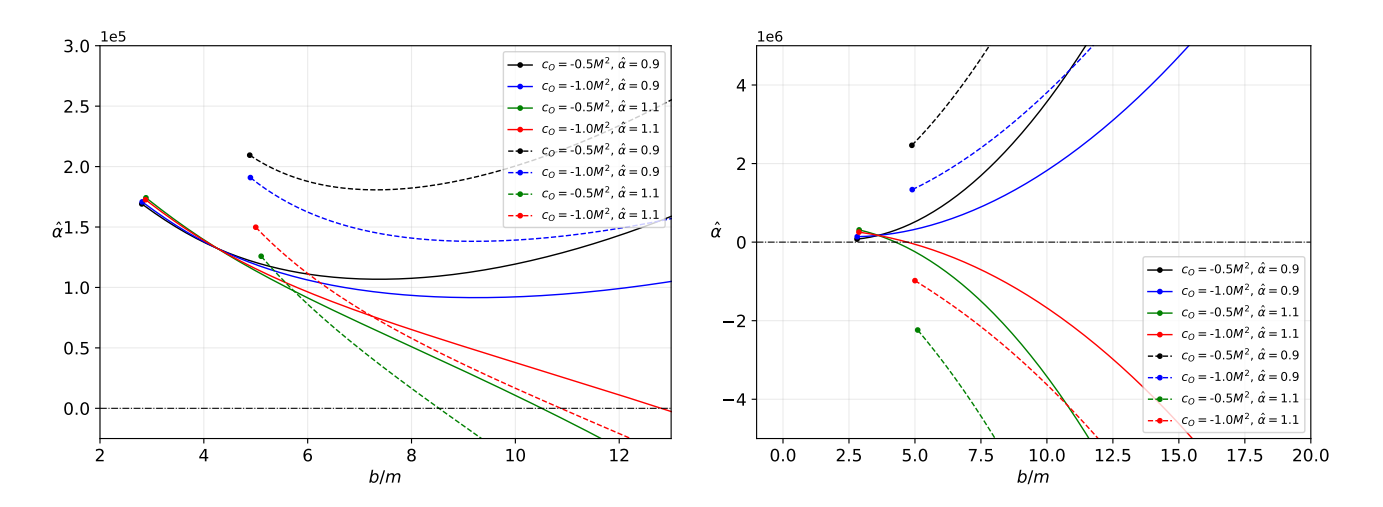


FIG. 8. Weak deflection angle of photons as a function of b/m for various values of the spin and symmergent parameters. The solid lines correspond to a>0 (prograde) and dashed lines correspond to a<0 (retrograde). In making these plots we take $u_{\rm S}=u_{\rm R}=0.5b^{-1}$ (left), $u_{\rm S}=u_{\rm R}=0.01b^{-1}$ (right), and $\hat{\alpha}=0.90$. The horizontal dotted lines represent critical impact parameters in each case.

Combining the above equations, we get an expression of the light deflection angle given by

$$\hat{\theta} = \left(\sqrt{1 - b^2 u_{\mathsf{R}}^2} + \sqrt{1 - b^2 u_{\mathsf{S}}^2}\right) \frac{2M}{b} - \left(\sqrt{1 - b^2 u_{\mathsf{R}}^2} - \sqrt{1 - b^2 u_{\mathsf{S}}^2}\right) \frac{2aM}{b^2} \\
- \left(\frac{1 - b^2 u_{\mathsf{R}}^2}{u_{\mathsf{R}} \sqrt{1 - b^2 u_{\mathsf{R}}^2}} + \frac{1 - b^2 u_{\mathsf{S}}^2}{u_{\mathsf{S}} \sqrt{1 - b^2 u_{\mathsf{S}}^2}}\right) \frac{b}{6} \frac{(1 - \hat{\alpha})}{8\pi c_0} + \left(\frac{1}{\sqrt{1 - b^2 u_{\mathsf{R}}^2}} + \frac{1}{\sqrt{1 - b^2 u_{\mathsf{S}}^2}}\right) \frac{bM}{6} \frac{(1 - \hat{\alpha})}{8\pi c_0} \\
+ \left(\frac{\sqrt{1 - b^2 u_{\mathsf{R}}^2}}{u_{\mathsf{R}}} + \frac{\sqrt{1 - b^2 u_{\mathsf{S}}^2}}{u_{\mathsf{S}}}\right) \frac{2a}{3} \frac{(1 - \hat{\alpha})}{8\pi c_0} + \mathcal{O}\left[M^2, \left(\frac{1 - \hat{\alpha}}{8\pi c_0}\right)^2, a^2\right]. \tag{72}$$

This form can be reduced to a simplified one using certain convenable approximations. Taking $u_S b << 1$ and $u_R b << 1$, we can get an expression involving divergent terms coupled to the cosmological contributions. These terms should be existed to show the cosmological background dependence. The desired deflection angle of light rays is found to be

$$\hat{\theta} = \frac{4M}{b} - \frac{4aM}{b^2} + \frac{bM}{3} \frac{(1-\hat{\alpha})}{8\pi c_0} - \left(\frac{1}{u_{\mathsf{R}}} + \frac{1}{u_{\mathsf{S}}}\right) \frac{b}{6} \frac{(1-\hat{\alpha})}{8\pi c_0} + \left(\frac{1}{u_{\mathsf{R}}} + \frac{1}{u_{\mathsf{S}}}\right) \frac{2a}{3} \frac{(1-\hat{\alpha})}{8\pi c_0} + \mathcal{O}\left[M^2, \left(\frac{1-\hat{\alpha}}{8\pi c_0}\right)^2, a^2\right] . \tag{73}$$

An examination shows that this expression recovers many previous findings. Without the cosmological contributions, we get the results of the ordinary Symmergent black hole solutions investigated in [22].

Plotted in Fig. 8 are the equations (72) (left-panel) and (73) (right-panel). The solid curves represent photons co-rotating with the black hole, while the dashed curves represent the counter-rotating photons. For the left-panel, which holds for finite distance, the results show that the co-rotating photons produce weak deflection angle at lower impact parameters compared to the counter-rotating photons. If we compare $\hat{\theta}$ for a specific orbital direction of photons, we see that the symmergent AdS type gives a higher value for $\hat{\theta}$ at large impact parameters. However, AdS type in the counter-rotation case gives a higher $\hat{\theta}$ than the co-rotation case. Finally, the right-panel stands for the case where we used the large distance approximation. Since the symmergent parameters are scaled, the location of the receiver in this case is comparable to the cosmic horizon. In this case, the symmergent effect is strong, giving the effects shown in the plot. We could see that there are cases where $\hat{\theta}$ is repulsive. In general, weak deflection angle is seen to have a strong sensitivity to the symmergent parameters.

VI. PARTICLE ACCELERATION NEAR ROTATING SYMMERGENT BLACK HOLE BACKGROUNDS

It turns out that collisions in equatorial plane near a Kerr black hole can occur with an arbitrarily high center of mass-energy [121–123]. In the present work, we find that the symmetre parameter c_0 has an important effect on the result. To do

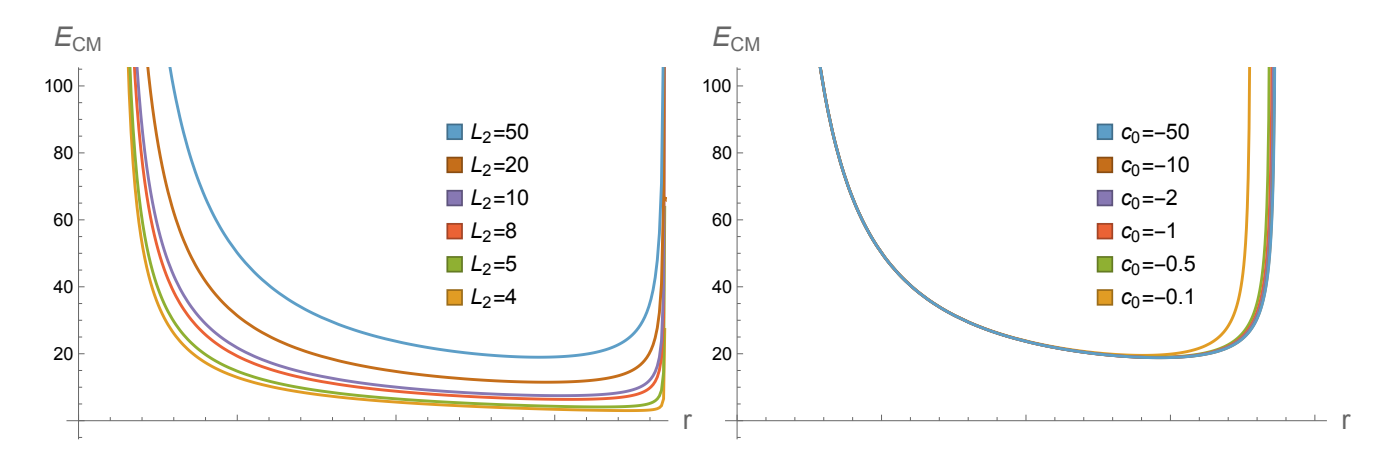


FIG. 9. Dependence of the CM energy $E_{\rm CM}$ on the radial distance r for different values of the spin and symmergent parameters. We consider two parameter sets $m=M=1,~L_1=-4,c_0=-0.5,~\hat{\alpha}=0.9$ and a=0.5 (left-panel) as well as $m=M=1,~L_1=-4,L_2=50,~\hat{\alpha}=0.9$ and a=0.5 (right-panel). It is clear that the CM energy blows up at the horizons.

that first we consider the particle motion on the equatorial plane $(\theta = \frac{\pi}{2}, \rho^2 = r^2)$. In fact, generalized momenta P_{μ} can be written as $(\mu, \nu = t, r, \phi, \theta)$

$$P_{\mu} = g_{\mu\nu}\dot{x}^{\nu} \tag{74}$$

where the dot stands for derivative with respect to the affine parameter λ . Then, one can write the generalized momenta P_t (test particle's energy per unit mass E) and P_{ϕ} (the angular momentum per unit mass L parallel to the symmetry axis)

$$P_t = g_{tt}\dot{t} + g_{t\phi}\dot{\phi},\tag{75}$$

$$P_{\phi} = g_{\phi\phi}\dot{\phi} + g_{t\phi}\dot{t} \tag{76}$$

where one keeps in mind that P_t and P_{ϕ} are constants of motion.

Our goal is to study the CM energy of the two-particle collision in the background spacetime of the rotating symmergent black holes. To this end, we start with the CM energy E_{CM} [121]

$$E_{\mathsf{CM}}^2 = 2m_0^2 \left(1 - g_{\mu\nu} u_1^{\mu} u_2^{\nu} \right) \tag{77}$$

in which u_1^μ, u_2^ν are the 4-velocity vectors of the two particles $(u=(\dot t,\dot r,0,\dot\phi))$. Correspondingly, particle i=1,2 has angular momentum per unit mass L_i and energy per unit mass E_i . We also consider particles with the same rest mass m_0 . Initially the two particles are at rest at infinity $(E_1/m_0=1)$ and $E_2/m_0=1$ and then they approach the black hole and collide at a distance r. Then, their CM energy takes the form

$$E_{\mathsf{CM}}^{2} = \frac{2m_{0}^{2}}{\Delta_{r}r^{2}} \left[\left(r^{2} + a^{2} \right)^{2} - a\left(L_{1} + L_{2} \right) \left(r^{2} + a^{2} - \Delta_{r} \right) + L_{1}L_{2} \left(a^{2} - \Delta_{r} \right) + \Delta_{r} \left(r^{2} - a^{2} \right) - X_{1}X_{2} \right]$$
(78)

with the functions

$$X_{i} = \sqrt{(aL_{i} - r^{2} - a^{2})^{2} - \Delta_{r} \left((L_{i} - a)^{2} + \mu^{2} r^{2} \right)}.$$
 (79)

Collisions occur at the horizon of the black hole so that $\Delta_r=0$ in equation (78). It is not difficult to see that the denominator of \bar{E}_{CM}^2 is zero there. Evidently, the maximal energy of the collision occurs if L_1 and L_2 are opposite (such as head-on collision). Plotted in Fig. VI is E_{CM} as a function of the radial distance r. As is seen from the figure, CM energy blows up at the horizons.

VII. CONCLUSION

In this paper, we have performed a detailed analysis of the symmergent gravity for different spinning black hole features. We have first investigated the effects of symmergent gravity on the photonsphere, black hole shadow, and certain observables

related to them. Our findings show that location of the photonsphere depends on the symmergent effects due to its coupling to the black hole spin parameter. We have seen how the unstable photon radii depend and get affected by c_0 and $\hat{\alpha}$. Also, symmergent gravity effect is evident, even for observers deviating from the equatorial plane. Interesting effects are also seen in the energy emission rate, which may directly affect the black hole's lifetime. Constraints on symmergent parameters from the shadow radius data coming from recent observations are also discussed. For a low and high spin parameter a values (the parameter $\hat{\alpha}$ dictates whether the symmergent effect mimics the dS and AdS type), we found that the parameter c_0 fits within $\pm 2\sigma$ at 95% confidence level for M87* than in Sgr. A*. It means that the true value is somewhere within such confidence level. The plot in Fig. 5 reveals that the detection of symmergent effects can be achieved more easily in M87* than in Sgr. A*, for the obvious reason that the farther the galaxy is the stronger the symmergent effects are. Finally, for comparison, we also briefly analyzed such an effect on the time-like geodesic. Our findings indicate that massive particles are more sensitive to deviations caused by the symmergent parameter than null particles.

In addition, we investigated the symmergent effects on photons' weak deflection angle as they traverse near the black hole. We also considered the finite distance effects. We have found that the deflection angle depends on $\hat{\alpha}$ but the deviations are also caused by how far the receiver is from the black hole. This effect is clearly shown in Fig. 8. It implies that the weak deflection angle can detect symmergent effects more easily for black holes that are significantly remote compared to our location.

Lastly, we study the particle collision near the rotating symmergent black hole background. We show that rotating symmergent black holes can serve as particle accelerators because the center-of-mass energies blow up at the horizons. As a result, the BSW mechanism depends on the value of the Symmergent parameter c_0 of the black hole.

Future research direction may include investigation of the shadow, and showing its dependence on the observer's state. One may also study the spherical photon orbits or the stability of time-like orbits.

ACKNOWLEDGMENTS

We thank to conscientious referee for their comments, questions and criticisms. We thank Xiao-Mei Kuang for useful discussions. A. Ö. acknowledges hospitality at Sabancı University where this work was completed. A. Ö. would like to acknowledge the contribution of the COST Action CA18108- Quantum gravity phenomenology in the multi-messenger approach (QG-MM).

- [1] I. Çimdiker, D. Demir, and A. Övgün, Phys. Dark Univ. 34, 100900 (2021), 2110.11904.
- [2] A. Macias and A. Camacho, Phys. Lett. B 663, 99 (2008).
- [3] R. M. Wald, Einstein Stud. 14, 439 (2018), 0907.0416.
- [4] F. Dyson, Int. J. Mod. Phys. A 28, 1330041 (2013).
- [5] G. 't Hooft and M. J. G. Veltman, Ann. Inst. H. Poincare Phys. Theor. A 20, 69 (1974).
- [6] A. D. Sakharov, Dokl. Akad. Nauk Ser. Fiz. 177, 70 (1967).
- [7] M. Visser, Mod. Phys. Lett. A 17, 977 (2002), gr-qc/0204062.
- [8] E. P. Verlinde, SciPost Phys. 2, 016 (2017), 1611.02269.
- [9] C. D. Froggatt and H. B. Nielsen, Annalen Phys. 517, 115 (2005), hep-th/0501149.
- [10] J. Polchinski, Nucl. Phys. B 231, 269 (1984).
- [11] H. Umezawa, J. Yukawa, and E. Yamada, Prog. Theor. Phys. 3, 317 (1948).
- [12] G. Kallen, Helv. Phys. Acta 22, 637 (1949).
- [13] D. Demir, Gen. Rel. Grav. 53, 22 (2021), 2101.12391.
- [14] P. W. Anderson, Phys. Rev. 130, 439 (1963).
- [15] F. Englert and R. Brout, Phys. Rev. Lett. 13, 321 (1964).
- [16] P. W. Higgs, Phys. Rev. Lett. 13, 508 (1964).
- [17] D. Demir, Adv. High Energy Phys. 2019, 4652048 (2019), 1901.07244.
- [18] D. A. Demir, Adv. High Energy Phys. 2016, 6727805 (2016), 1605.00377.
- [19] N. D. Birrell and P. C. W. Davies, Quantum Fields in Curved Space, Cambridge Monographs on Mathematical Physics (Cambridge Univ. Press, Cambridge, UK, 1984), ISBN 978-0-521-27858-4, 978-0-521-27858-4.
- [20] D. Demir, Galaxies 9, 33 (2021), 2105.04277.
- [21] I. I. Çimdiker, Phys. Dark Univ. 30, 100736 (2020).
- [22] J. Rayimbaev, R. C. Pantig, A. Övgün, A. Abdujabbarov, and D. Demir (2022), 2206.06599.
- [23] K. S. Virbhadra and G. F. R. Ellis, Phys. Rev. D **62**, 084003 (2000), astro-ph/9904193.
- [24] K. S. Virbhadra and G. F. R. Ellis, Phys. Rev. D 65, 103004 (2002).
- [25] K. S. Virbhadra, D. Narasimha, and S. M. Chitre, Astron. Astrophys. 337, 1 (1998), astro-ph/9801174.
- [26] K. S. Virbhadra and C. R. Keeton, Phys. Rev. D 77, 124014 (2008), 0710.2333.

- [27] K. S. Virbhadra, Phys. Rev. D 79, 083004 (2009), 0810.2109.
- [28] S. L. Adler and K. S. Virbhadra (2022), 2205.04628.
- [29] V. Bozza, S. Capozziello, G. Iovane, and G. Scarpetta, Gen. Rel. Grav. 33, 1535 (2001), gr-qc/0102068.
- [30] V. Bozza, Phys. Rev. D 66, 103001 (2002), gr-qc/0208075.
- [31] V. Perlick, Phys. Rev. D 69, 064017 (2004), gr-qc/0307072.
- [32] G. He, X. Zhou, Z. Feng, X. Mu, H. Wang, W. Li, C. Pan, and W. Lin, Eur. Phys. J. C 80, 835 (2020).
- [33] K. S. Virbhadra (2022), 2204.01792.
- [34] K. S. Virbhadra (2022), 2204.01879.
- [35] G. W. Gibbons and M. C. Werner, Class. Quant. Grav. 25, 235009 (2008), 0807.0854.
- [36] A. Övgün, Phys. Rev. D 98, 044033 (2018), 1805.06296.
- [37] A. Övgün, Phys. Rev. D 99, 104075 (2019), 1902.04411.
- [38] A. Övgün, Universe 5, 115 (2019), 1806.05549.
- [39] W. Javed, R. Babar, and A. Övgün, Phys. Rev. D 100, 104032 (2019), 1910.11697.
- [40] M. C. Werner, Gen. Rel. Grav. 44, 3047 (2012), 1205.3876.
- [41] A. Ishihara, Y. Suzuki, T. Ono, T. Kitamura, and H. Asada, Phys. Rev. D **94**, 084015 (2016), 1604.08308.
- [42] A. Ishihara, Y. Suzuki, T. Ono, and H. Asada, Phys. Rev. D 95, 044017 (2017), 1612.04044.
- [43] T. Ono, A. Ishihara, and H. Asada, Phys. Rev. D 96, 104037 (2017), 1704.05615.
- [44] R. C. Pantig and E. T. Rodulfo, Chin. J. Phys. 66, 691 (2020), 2003.00764.
- [45] R. C. Pantig, P. K. Yu, E. T. Rodulfo, and A. Övgün, Annals of Physics 436, 168722 (2022), 2104.04304.
- [46] R. C. Pantig and A. Övgün, Eur. Phys. J. C 82, 391 (2022), 2201.03365.
- [47] Z. Li and A. Övgün, Phys. Rev. D 101, 024040 (2020), 2001.02074.
- [48] Z. Li, G. Zhang, and A. Övgün, Phys. Rev. D 101, 124058 (2020), 2006.13047.
- [49] A. Belhaj, H. Belmahi, M. Benali, and H. Moumni El (2022), 2204.10150.
- [50] S. Vagnozzi, R. Roy, Y.-D. Tsai, and L. Visinelli (2022), 2205.07787.
- [51] Y. Chen, R. Roy, S. Vagnozzi, and L. Visinelli (2022), 2205.06238.
- [52] R. C. Pantig and E. T. Rodulfo, Chinese J. Phys. **68**, 236 (2020).
- [53] I. Dymnikova and K. Kraav, Universe **5**, 1 (2019), ISSN 22181997.
- [54] R. C. Pantig and A. Övgün, JCAP **08**, 056 (2022), 2202.07404.
- [55] A. Uniyal, R. C. Pantig, and A. Övgün (2022), 2205.11072.
- [56] X.-M. Kuang and A. Övgün (2022), 2205.11003.
- [57] Y. Meng, X.-M. Kuang, and Z.-Y. Tang (2022), 2204.00897.
- [58] Z.-Y. Tang, X.-M. Kuang, B. Wang, and W.-L. Qian (2022), 2206.08608.
- [59] X.-M. Kuang, Z.-Y. Tang, B. Wang, and A. Wang (2022), 2206.05878.
- [60] R. C. Pantig and A. Övgün (2022), 2206.02161, URL https://arxiv.org/abs/2206.02161.
- [61] S.-W. Wei, Y.-C. Zou, Y.-X. Liu, and R. B. Mann, JCAP **08**, 030 (2019), 1904.07710.
- [62] Z. Xu, X. Hou, and J. Wang, JCAP 10, 046 (2018), 1806.09415.
- [63] X. Hou, Z. Xu, and J. Wang, JCAP 12, 040 (2018), 1810.06381.
- [64] C. Bambi, K. Freese, S. Vagnozzi, and L. Visinelli, Phys. Rev. D 100, 044057 (2019), 1904.12983.
- [65] N. Tsukamoto, Phys. Rev. D 97, 064021 (2018), 1708.07427.
- [66] R. Kumar, S. G. Ghosh, and A. Wang, Phys. Rev. D **101**, 104001 (2020), 2001.00460.
- [67] R. Kumar, S. G. Ghosh, and A. Wang, Phys. Rev. D 100, 1 (2019), ISSN 24700029, 1912.05154.
- [68] M. Wang, S. Chen, and J. Jing, J. Cosmol. Astropart. Phys. 2017, 1 (2017), ISSN 14757516, 1707.09451.
- [69] M. Wang, S. Chen, and J. Jing, Phys. Rev. D 98, 1 (2018), ISSN 24700029, 1801.02118.
- [70] L. Amarilla and E. F. Eiroa, 14th Marcel Grossman Meet. Recent Dev. Theor. Exp. Gen. Relativ. Astrophys. Relativ. F. Theor. Proc. -, 3543 (2018), 1512.08956.
- [71] H. Peng-Zhang, F. Qi-Qi, Z. Hao-Ran, and D. Jian-Bo, Eur. Phys. J. C 80, 1195 (2020).
- [72] O. Y. Tsupko, Z. Fan, and G. S. Bisnovatyi-Kogan, Class. Quant. Grav. 37, 065016 (2020), 1905.10509.
- [73] K. Hioki and K.-i. Maeda, Phys. Rev. D 80, 024042 (2009), 0904.3575.
- [74] R. A. Konoplya, Phys. Lett. B 795, 1 (2019), 1905.00064.
- [75] R. C. Pantig, in Proceedings of the Samahang Pisika ng Pilipinas (2021), vol. 39, pp. SPP-2021-1C-03.
- [76] M. Okyay and A. Övgün, JCAP **01**, 009 (2022), 2108.07766.
- . 1771 A. Belhai, M. Benali, A. El Balali, H. El Moumni, and S. E. Ennadifi, Class. Quant. Grav. 37, 215004 (2020), 2006.01078.
- [78] P.-C. Li, M. Guo, and B. Chen, Phys. Rev. D 101, 084041 (2020), 2001.04231.
- [79] R. Ling, H. Guo, H. Liu, X.-M. Kuang, and B. Wang, Phys. Rev. D 104, 104003 (2021), 2107.05171.
- [80] A. Belhaj, H. Belmahi, M. Benali, W. El Hadri, H. El Moumni, and E. Torrente-Lujan, Phys. Lett. B 812, 136025 (2021), 2008.13478.
- [81] P. V. P. Cunha and C. A. R. Herdeiro, Gen. Rel. Grav. 50, 42 (2018), 1801.00860.
- [82] S. E. Gralla, D. E. Holz, and R. M. Wald, Phys. Rev. D 100, 024018 (2019), 1906.00873.
- [83] V. Perlick, O. Y. Tsupko, and G. S. Bisnovatyi-Kogan, Phys. Rev. D 92, 104031 (2015), 1507.04217.
- [84] P. G. Nedkova, V. K. Tinchev, and S. S. Yazadjiev, Phys. Rev. D 88, 124019 (2013), 1307.7647.
- [85] Z. Li and C. Bambi, JCAP **01**, 041 (2014), 1309.1606.
- [86] M. Khodadi, G. Lambiase, and D. F. Mota, JCAP 09, 028 (2021), 2107.00834.

- [87] M. Khodadi and G. Lambiase (2022), 2206.08601.
- [88] P. V. P. Cunha, C. A. R. Herdeiro, B. Kleihaus, J. Kunz, and E. Radu, Phys. Lett. B 768, 373 (2017), 1701.00079.
- [89] R. Shaikh, Phys. Rev. D 100, 024028 (2019), 1904.08322.
- 90 A. Allahyari, M. Khodadi, S. Vagnozzi, and D. F. Mota, JCAP **02**, 003 (2020), 1912.08231.
- [91] A. Yumoto, D. Nitta, T. Chiba, and N. Sugiyama, Phys. Rev. D 86, 103001 (2012), 1208.0635.
- [92] P. V. P. Cunha, C. A. R. Herdeiro, E. Radu, and H. F. Runarsson, Int. J. Mod. Phys. D **25**, 1641021 (2016), 1605.08293.
- [93] J. W. Moffat, Eur. Phys. J. C 75, 130 (2015), 1502.01677.
- 94] P. V. P. Cunha, J. Grover, C. Herdeiro, E. Radu, H. Runarsson, and A. Wittig, Phys. Rev. D 94, 104023 (2016), 1609.01340.
- [95] A. F. Zakharov, Phys. Rev. D **90**, 062007 (2014), 1407.7457.
- 96 R. A. Hennigar, M. B. J. Poshteh, and R. B. Mann, Phys. Rev. D **97**, 064041 (2018), 1801.03223.
- [97] L. Chakhchi, H. El Moumni, and K. Masmar, Phys. Rev. D 105, 064031 (2022).
- [98] J. L. Synge, Mon. Not. R. Astron. Soc. 131, 463 (1966), ISSN 0035-8711.
- [99] J. P. Luminet, Astron. Astrophys. **75**, 228 (1979).
- [100] J. M. Bardeen, in Les Houches Summer School of Theoretical Physics: Black Holes (1973), pp. 215-240.
- [101] S. Chandrasekhar, The mathematical theory of black holes (Oxford University Press., New York, 1998).
- [102] B. P. Abbott et al. (LIGO Scientific, Virgo), Phys. Rev. Lett. 116, 061102 (2016), 1602.03837.
- [103] K. Akiyama et al. (Event Horizon Telescope), Astrophys. J. Lett. 875, L6 (2019), 1906.11243.
- [104] K. Akiyama et al. (Event Horizon Telescope), Astrophys. J. Lett. 930, L12 (2022).
- [105] J. A. R. Cembranos, A. de la Cruz-Dombriz, and P. Jimeno Romero, Int. J. Geom. Meth. Mod. Phys. 11, 1450001 (2014), 1109.4519.
- [106] S. Dastan, R. Saffari, and S. Soroushfar, Eur. Phys. J. Plus 137, 1002 (2022), 1606.06994.
- [107] D. Perez, G. E. Romero, and S. E. P. Bergliaffa, Astron. Astrophys. 551, A4 (2013), 1212.2640.
- [108] A. G. Suvorov, Phys. Rev. D 99, 124026 (2019), 1905.02021.
- [109] Y. S. Myung, Phys. Rev. D 88, 104017 (2013), 1309.3346.
- [110] G. L. L. Nashed and S. Nojiri, JCAP 11, 007 (2021), 2109.02638.
- [111] G. G. L. Nashed, Phys. Lett. B 815, 136133 (2021), 2102.11722.
- [112] G. W. Gibbons, M. J. Perry, and C. N. Pope, Class. Quant. Grav. 22, 1503 (2005), hep-th/0408217.
- [113] Z. Gao, X. Kong, and L. Zhao, Eur. Phys. J. C 82, 112 (2022), 2112.08672.
- [114] L. Pogosian and A. Silvestri, Phys. Rev. D 77, 023503 (2008), [Erratum: Phys.Rev.D 81, 049901 (2010)], 0709.0296.
- [115] P. Slany and Z. Stuchlik, Eur. Phys. J. C 80, 587 (2020).
- [116] B. Carter, Phys. Rev. 174, 1559 (1968).
- [117] T. Johannsen, Astrophys. J. 777, 170 (2013).
- [118] K. Akiyama et al. (Event Horizon Telescope), Astrophys. J. Lett. 875, L1 (2019), 1906.11238.
- [119] B. Bautista-Olvera, J. C. Degollado, and G. German, arXiv preprint arXiv:1908.01886 pp. 1-18 (2019), 1908.01886.
- [120] P. Slaný, M. Pokorná, and Z. Stuchlík, Gen. Relativ. Gravit. 45, 2611 (2013), ISSN 00017701, 0307049.
- [121] M. Banados, J. Silk, and S. M. West, Phys. Rev. Lett. 103, 111102 (2009), 0909.0169.
- [122] M. Halilsoy and A. Ovgun, Adv. High Energy Phys. 2017, 4383617 (2017), 1504.03840.
- [123] M. Halilsoy and A. Ovgun, Can. J. Phys. 95, 1037 (2017), 1507.00633.